Nanoscale

Biomass-derived nitrogen self-doped porous carbon as effective metal-free catalysts for oxygen reduction reaction†

Xiaojun Liu,[a] Yucheng Zhou,[a] Weijia Zhou,*[a] Ligui Li,[a] Shaobin Huang[a] and Shaowei Chen*[a,b]

Biomass-derived nitrogen self-doped porous carbon was synthesized by a facile procedure based on simple pyrolysis of water hyacinth (*eichhornia crassipes*) at controlled temperatures (600–800 °C) with $ZnCl_2$ as an activation reagent. The obtained porous carbon exhibited a BET surface area up to 950.6 m^2 g^{-1}, and various forms of nitrogen (pyridinic, pyrrolic and graphitic) were found to be incorporated into the carbon molecular skeleton. Electrochemical measurements showed that the nitrogen self-doped carbons possessed a high electrocatalytic activity for ORR in alkaline media that was highly comparable to that of commercial 20% Pt/C catalysts. Experimentally, the best performance was identified with the sample prepared at 700 °C, with the onset potential at *ca.* +0.98 V *vs.* RHE, that possessed the highest concentrations of pyridinic and graphitic nitrogens among the series. Moreover, the porous carbon catalysts showed excellent long-term stability and much enhanced methanol tolerance, as compared to commercial Pt/C. The performance was also markedly better than or at least comparable to the leading results in the literature based on biomass-derived carbon catalysts for ORR. The results suggested a promising route based on economical and sustainable biomass towards the development and engineering of value-added carbon materials as effective metal-free cathode catalysts for alkaline fuel cells.

Introduction

A critical issue in the commercialization of fuel cells and metal–air batteries is the development of highly efficient, cost-effective catalysts for oxygen reduction reaction (ORR) at the cathode. Thus far, platinum and its alloys have been the best electrocatalysts for accelerating the ORR process.[1] However, Pt is both expensive and scarce, which greatly impedes its widespread implementation in fuel cells. Moreover, Pt-based catalysts are susceptible to potential drifting during operation; and methanol crossover causes mixed potentials at the fuel cell cathode. Thus, extensive research efforts have been devoted to catalyst design and engineering by decreasing the Pt content and/or replacing Pt with less expensive materials.

Heteroatom-doped carbon nanomaterials have been discovered as promising contenders for ORR electrocatalysis with regard to their wide availability, corrosion resistance, and environmentally benign nature.[2,3] In fact, carbon doped with single,[4,5] dual,[6,7] or multiple heteroatoms[8] into its molecular framework has showed efficacy as a Pt-free electrocatalyst in a series of studies. Recently, the research focus has shifted from expensive, often hazardous inorganic and organic chemicals to renewable natural resources as precursors in the preparation of functional carbon nanomaterials as ORR catalysts.

Towards this end, biomass is an attractive starting material which is generally cheap, readily available in high quality and quantity, and environmental friendly. In addition to its carbon and water content, biomass is rich in elements such as sulfur, nitrogen, and phosphorus, as well as metals such as Fe, Cu, and others. It is thus reasonable to expect that controlled pyrolysis of biomass might lead to the production of doped carbons as high-performance ORR catalysts.[9] In fact, some progress has been made along this direction where carbons of high surface areas were synthesized from, for instance, crab shells[10] and pig bones.[11] N-doped carbon materials have also been prepared from egg-white protein,[12] pork liver,[13] amaranth,[14] and ginkgo leaves,[15] and used as effective electrode materials for supercapacitors or ORR. In a more recent study,

[a] New Energy Research Institute, School of Environment and Energy, South China University of Technology, Guangzhou Higher Education Mega Center, Guangzhou, Guangdong 510006, China. E-mail: eszhouwj@scut.edu.cn, shaowei@ucsc.edu
[b] Department of Chemistry and Biochemistry, University of California, 1156 High Street, Santa Cruz, California 95064, USA
†Electronic supplementary information (ESI) available: Additional SEM, TEM and electrochemical data, and comparison of ORR performance with other biomass-derived carbons in the literature. See DOI: 10.1039/c5nr00013k

(N and S) dual-doped highly conductive carbons were prepared by pyrolysis of human hair, which exhibited a high surface area and remarkable ORR activity. These prior studies highlight the untapped potential of organic-rich wastes in the development of metal-free ORR catalysts.[16]

Eichhornia crassipes, a typical biomass feedstock, commonly known as water hyacinth, is an aquatic plant native to the Amazon basin. It can be widely found in North America, Asia, Australia, Africa and New Zealand, and is a worldwide aquatic weed species with a high reproductive ability. The free-floating perennial plant contains about 30% protein, which comes mainly from amino acids, such as lysine, leucine, tyrosine and valine.[17–19] Moreover, it has the ability to accumulate appreciable amounts of the inorganic forms of nitrogen found in domestic sewage.[19] Such unique characteristics might be exploited in the preparation of heteroatom-doped carbon. This is the primary motivation of the present study.

Herein we describe a low-cost, simple and readily scalable approach for the synthesis of N-doped porous carbon from water hyacinth by a facile pyrolysis process at controlled temperature with $ZnCl_2$ as the activation reagent. The unique advantages of the synthetic strategy include the following: (i) naturally sustainable biomass that contains a large amount of organic and inorganic nitrogen is used as precursors; (ii) the synthetic procedure is simple and scalable without the need of additional templates, and (iii) the resulting biomass-derived carbons exhibit a high BET surface area, hierarchical porous distribution, uniform nitrogen doping, as well as high contents of pyridinic and graphitic nitrogen species. Electrochemical measurements of the obtained porous carbons showed excellent catalytic ability for ORR in alkaline media with remarkable stability and tolerance to methanol poisoning effects, a performance that was highly comparable to that of leading commercial Pt/C catalysts. To the best of our knowledge, this is the first report where N-doped porous carbons were prepared from water hyacinth and used as an effective metal-free catalyst for ORR.

Experimental section

Materials

All the reagents were of analytical grade and used without further purification. Water hyacinth was obtained from a local wetland in Guangzhou, washed with distilled water and crushed. $ZnCl_2$ (98.0%) was purchased from Da Mao Company (Nanjing).

Preparation of N self-doped porous carbon

The procedure of the preparation of porous carbons from water hyacinth was summarized in Scheme 1. Before heat treatment the water hyacinth were carefully washed with DI-water, cut into small pieces (about 1 cm long), and dried under vacuum at 80 °C for 12 h. The dried samples were then ground to powders in a mortar, and heated with the addition of $ZnCl_2$ (mass ratio of $ZnCl_2$–water hyacinth 1 : 6) under N_2 at an

Scheme 1 Schematic of the synthesis of N self-doped porous carbon from water hyacinth.

elevated temperature between 600 and 800 °C for 2 h. When cooled down to room temperature, the samples were rinsed extensively with 0.5 M HNO_3 and 1 M HCl to remove possible metal deposits, before being filtered, thoroughly washed with DI-water, and then dried in an oven at 80 °C. The obtained water hyacinth derived-porous carbons were denoted as WHC-T, where T denoted the pyrolysis temperature (600, 700, and 800 °C).

Characterization

The morphology was examined with a field emission scanning electron microscope (FE SEM, Zeiss) and a high-resolution transmission electron microscope (HRTEM, JEOL JEM-2010). X-ray powder diffraction (XRD) patterns in the Bragg's angle (2θ) range of 15 to 80° were collected at room temperature using a Bruker D_8 diffractometer with Cu Kα radiation ($\lambda = 0.1541$ nm). Raman spectra were acquired on a LabRAM HR Evolution system equipped with a deep-depleted thermoelectrically cooled CCD array detector, an Ar laser ($\lambda = 514.5$ nm) and long working distance 50× objective lens. Nitrogen adsorption–desorption isotherms were measured at 77 K using an ASAP 2020-Physisorption Analyzer (Micromeritics, USA) where the BET method was used for surface area determination. The pore size distribution (PSD) was calculated *via* a density function theory (DFT) method by using nitrogen adsorption data and assuming a slit pore model. X-ray photoelectron spectroscopic (XPS) measurements were conducted with a VG Microtech ESCA 2000 using a monochromic Al X-ray source.

Electrochemistry

Electrochemical experiments were conducted at room temperature on a CHI660E electrochemical workstation (CH instrument Co.) with a three-electrode cell equipped with gas-flow systems. A Pt foil and Ag/AgCl (3 M KCl) were used as the counter electrode and reference electrode, respectively. The working electrode was a rotating ring-disk electrode with a glassy carbon disk (5.61 mm in diameter, with a collection efficiency of 37%). Experimentally, 2.0 mg of the porous

carbons prepared above was added into 1 mL of ethanol and 10 µL of a Nafion solution (5 wt%, Aldrich) and sonicated for 30 min to form a well-dispersed ink, 20 µL of which was then transferred onto the surface of the glassy carbon electrode and then dried at room temperature for 20 min to obtain a catalyst thin film. Commercial Pt/C was loaded onto the electrode surface in a similar fashion. For ORR measurements, the electrolyte was pre-saturated with O_2 for 30 min prior to data acquisition. RDE linear sweep voltammetry was performed in an O_2-saturated 0.1 M KOH solution at a scan rate of 10 mV s^{-1} from -1.0 V to $+0.2$ V at different rotation speeds from 100 to 2500 rpm. The potential of the reference electrode was calibrated with a reversible hydrogen electrode (RHE), and in 0.1 M KOH, $E_{Ag/AgCl} = E_{RHE} + 0.982$ V.[20] The geometrical area of the electrode was used to calculate the current density.

Results and discussion

The structures of the obtained carbon samples were first characterized by electron microscopic measurements. Fig. 1 depicts the representative SEM and TEM images of the WHC-700 sample. From panel (a) one can see that the obtained carbon exhibited an irregular shape with a rather rough surface, and high-magnification SEM studies in panel (b) revealed that the sample actually consisted of a loose, porous structure formed by agglomeration of sheet-like particles. The morphology and structure was further examined by TEM studies. As shown in panels (c) and (d), it can be seen that the WHC-700 sample displayed a spongy and porous structure, suggesting a large specific surface area. Similar structures were obtained with samples prepared at other pyrolysis temperatures (Fig. S1†).
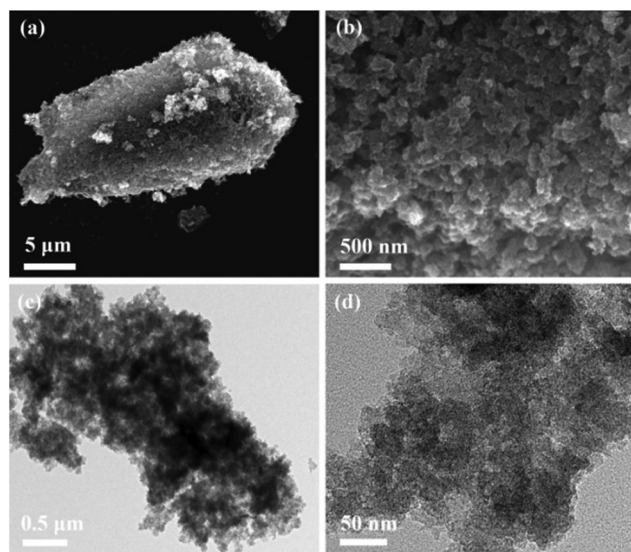

Fig. 1 Representative (a and b) SEM and (c and d) TEM images of the WHC-700 sample.
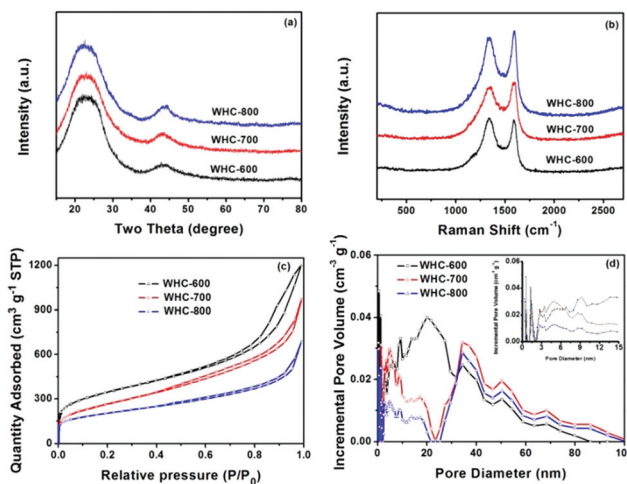

Fig. 2 (a) XRD patterns, (b) Raman spectra, (c) nitrogen adsorption–desorption isotherms and (d) pore size distribution of WHC-600, WHC-700, and WHC-800. The inset to panel (d) shows the enlarged portion of the pore-size distributions of the three samples.

Fig. 2a shows the wide-angle XRD patterns of the WHCs prepared at 600, 700 and 800 °C, which all exhibited two broad peaks centered at 23.8° and 43.8°, corresponding to the (002) and (100) lattice planes of typical turbostratic carbon. This suggests the formation of graphitic carbon.[21] Raman spectra of the samples were depicted in panel (b), with two prominent peaks centered at around 1345 and 1595 cm^{-1} that were the characteristic D and G bands of carbon materials, respectively. The D band is indicative of the disordered graphite structure, whereas the G band indicates the presence of the crystalline graphitic carbon, and the intensity ratio of the D and G bands (I_D/I_G) can be used to quantify the extent of disordering within the samples. From the spectra, the I_D/I_G ratio was estimated to be 1.12, 0.95, and 0.92 for WHC-600, WHC-700, and WHC-800, respectively, indicating a higher degree of structural alignment at higher carbonization temperature.

The specific surface area of the porous carbon was then quantified by nitrogen adsorption–desorption measurements. Panels (c) and (d) showed the nitrogen adsorption–desorption isotherms and pore-size distribution (PSD) of the three samples. It can be seen that all three samples showed a type-IV isotherm with a larger slope at higher relative pressures, which was commonly related to capillary condensation in mesopores.[22–24] The sharp increase at low pressures ($P/P_0 < 0.45$) indicated the existence of micropores. A hysteresis loop extending from $P/P_0 = 0.4$ to 0.85 was observed for WHC-700, suggesting the coexistence of both micropores and mesopores in the sample. Moreover, for all samples, the obvious tails appeared at $P/P_0 \sim 1.0$, indicating the formation of macropores within the carbons.[24,25] Consistent results were obtained in PSD studies where the PSD was calculated using the non-local density functional theory (NL-DFT) method. The results indicated the prevalence of micropores and small macropores

Table 1 Summary of results obtained from nitrogen adsorption–desorption analysis and chemical composition analysis from XPS measurements

Sample	S_{BET} $(m^2\ g^{-1})$	Pore volumes $(cm^3\ g^{-1})$	Average pore width (nm)	At% (C)	At% (N)	At% (O)
WHC-600	1199.3	1.88	6.20	87.82	5.02	7.13
WHC-700	950.6	1.49	6.33	85.56	4.76	9.67
WHC-800	700.6	1.09	6.10	88.05	2.80	9.15

ranging from 0.5 to 68.1 nm in size with a specific surface area of 1199.3, 950.6 and 700.6 $m^2\ g^{-1}$ for WHC-600, WHC-700, and WHC-800, respectively. The results are also summarized in Table 1. It can be seen that as the activation temperature increased from 600 to 800 °C, both the surface area and pore volume decreased dramatically, which was probably due to the collapse of pores and enhanced orientation during the activation process.[26]

XPS measurements were then carried out to examine the valence states and elemental compositions of the carbons. From the survey spectra in Fig. 3a, one can see that all samples exhibited only C 1s (ca. 284 eV), O 1s (ca. 532 eV), and N 1s (ca. 400 eV) electrons, confirming that the obtained samples were indeed N-doped carbons. Additionally, based on the integrated

peak areas, the level of nitrogen doping was estimated to be 5.02 at% for WHC-600, 4.76 at% for WHC-700, and 2.80 at% for WHC-800 (Table 1), suggesting a diminishing nitrogen loading at increasing pyrolysis temperature. The chemical structures of N dopants in the carbons were further probed by high-resolution scans, as depicted in panels (b) to (d). Deconvolutions of the spectra all yield three major components that are consistent with pyridinic N (398.4 ± 0.2 eV), pyrrolic N (399.9 ± 0.2 eV), and quaternary or graphitic N (401.2 ± 0.2 eV).[24,27–29] Based on the integrated peak areas, the fractions of each nitrogen components might be quantified, as shown in panel (e), where one can see that graphitic-N was the dominant species in all samples, 2.33% for WHC-600, 3.22% for WHC-700, and 2.63% for WHC-800, with WHC-700 possessing the highest concentration. Furthermore, within the pyrolysis temperatures range of 600 to 800 °C, the concentration of pyridinic N also reached the maximum of 1.40% at 700 °C, whereas the pyrrolic N content was markedly higher in WHC-600 (1.47%) than in WHC-700 (0.14%) and WHC-800 (0.06%), possibly due to its lower stability at higher temperatures.[30] Overall, the XPS results confirmed that indeed various N species were successfully incorporated into the carbon frameworks.

Note that graphitic and pyridinic nitrogens have been proposed as the key active sites for ORR.[31] Thus one may anticipate that the porous carbons obtained above would exhibit apparent electrocatalytic activity for ORR. Electrochemical measurements for WHC-600, WHC-700 and WHC-800 were then performed in a 0.1 M KOH solution saturated with N_2 or O_2 at the scan rate of 10 mV s^{-1}, as shown in Fig. 4a. It can be seen that in N_2-saturated KOH, the three carbon samples exhibited only a featureless double-layer charging voltammetric profile. In contrast, when the electrolyte solution was saturated with oxygen, a cathodic peak emerged at +0.78 V for WHC-600, +0.88 V for WHC-700, and +0.85 V for WHC-800, indicating apparent catalytic activity of the three carbon samples, and based on the peak potential, WHC-700 appeared to be the best catalyst among the series. Consistent results were obtained in RDE measurements at a rotation speed of 1600 rpm, along with commercial Pt/C catalysts, as shown in Fig. 4b. First, it can be seen that for all samples, when the electrode potential was swept negatively, nonzero cathodic currents started to appear where the onset potential was identified at +0.84 V for WHC-600, +0.98 V for WHC-700, +0.91 V for WHC-800. Of note is that the onset potential of WHC-700 was even more positive than that of commercial Pt/C (+0.95 V). At sufficiently negative electrode potentials (<+0.60 V), the currents reached a plateau; and the limiting current density varied. For instance, at +0.40 V, the limiting current density increased in the order of WHC-600 (2.78 mA cm^{-2}) < WHC-800 (3.57 mA cm^{-2}) < Pt/C (3.90 mA cm^{-2}) < WHC-700 (4.15 mA cm^{-2}), again, signifying that WHC-700 stood out as the best catalyst among the series (apparent ORR activity was also observed in acid solutions with WHC-700 exhibiting the best performance, Fig. S2†). This remarkable performance may be attributed to the unique nitrogen dopants in the porous
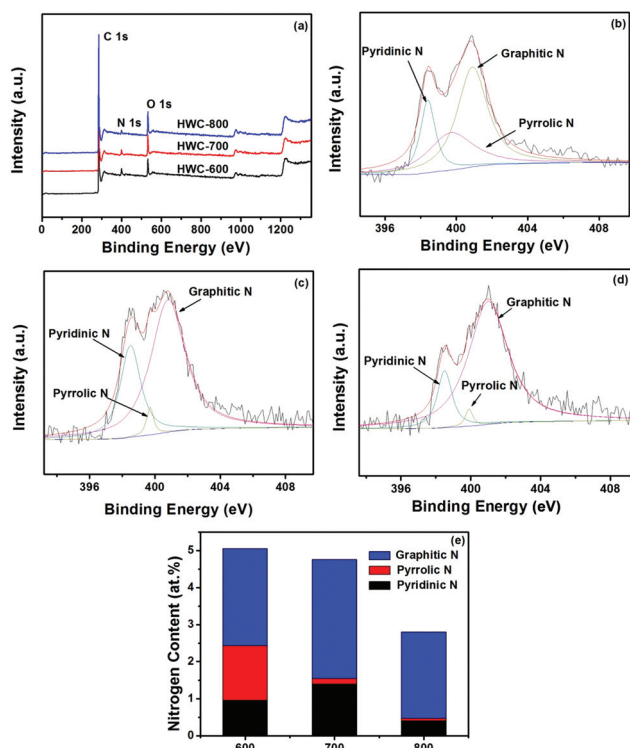
Fig. 3 (a) XPS survey spectra and high-resolution scans of N 1s electrons of (b) WHC-600, (c) WHC-700, and (d) WHC-800. (e) Nitrogen contents in the carbon samples.
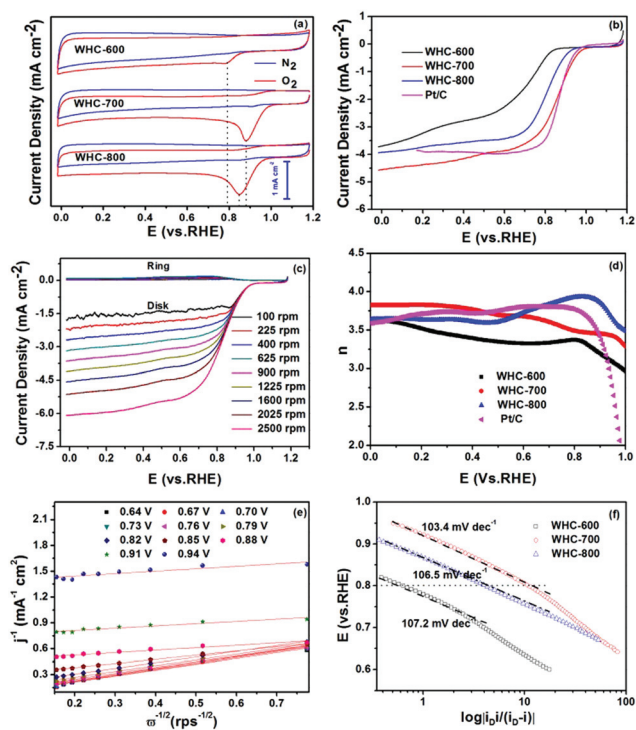
Fig. 4 (a) Cyclic voltammograms of WHC-600, WHC-700 and WHC-800 in N_2 and O_2-saturated 0.1 M KOH; (b) linear sweep voltammograms of WHC-600, WHC-700, WHC-800, and Pt/C RDE electrodes at 1600 rpm and 10 mV s^{-1}; (c) polarization curves for ORR in O_2-saturated 0.1 M KOH solution on WHC-700 electrode at various rotation rates, with the ring potential set at +0.5 V; (d) variation of number of electron transfer (n) with electrode potential for WHC-600, WHC-700, WHC-800 and Pt/C; (e) Koutecky–Levich plots of WHC-700 at different electrode potentials; (f) Tafel plots of WHC-600, WHC-700 and WHC-800.

carbons that enhanced the first electron transfer of oxygen reduction and the four-electron (rather than the two-electron) reduction pathway.[32] It has been reported in the literature that pyridinic and graphitic nitrogens play a predominant role in determining the electrochemical activity of carbon catalysts for ORR,[33,34] where graphitic N was thought to be responsible for the limiting current density and pyridinic N to determine the onset potential, while other N species such as pyrrolic N had little effect on the electrocatalytic performance of the carbon materials.[31] From the XPS measurements (Fig. 3), one can see that the WHC-700 sample indeed possessed the highest contents of pyridinic and graphitic N.[35] Moreover, the high surface area and mesoporous structure of WHC-700 was favorable for mass transfer of the reactants and products in ORR.[36]

To further examine the ORR activity, we also performed RRDE measurements at various rotation speeds (Fig. 4c and Fig. S3a, b†). It can be seen that the disk current density increased with increasing rotation rate (from 100 to 2500 rpm), and the ring currents were at least an order of magnitude lower, signifying a low concentration of peroxide species produced during ORR at the disk electrode. In fact, the
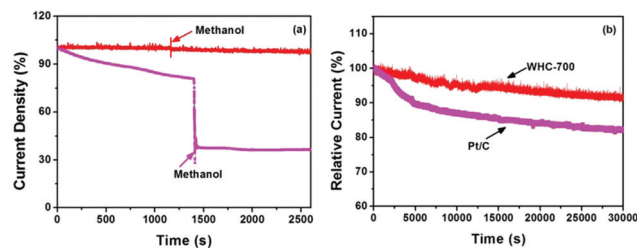

Fig. 5 (a) Current–time (i–t) responses for ORR at +0.4 V vs. RHE in an O_2-saturated 0.1 M KOH solution at WHC-700 and Pt/C modified electrode with the addition of 3 M methanol at 1200 s and 1400 s, which is marked with an arrow. (b) Stability evaluation of HPC-700 and Pt/C for 30 000 s in an O_2-saturated 0.1 M KOH solution at +0.4 V vs. RHE with a rotation speed of 900 rpm.

number of electron transfer (n) might be quantified on the basis of the disk current (I_{Disk}) and ring current (I_{Ring}),

$$n = \frac{4 I_{Disk}}{I_{Disk} + I_{Ring}/N} \quad (1)$$

where $N = 0.37$, the collection efficiency of the Pt ring. Fig. 5d displays the variation of n with electrode potentials. It can be seen that for WHC-600, n was 3.31–3.64 within the range of 0 to +0.85 V, which increased rather markedly to 3.51–3.82 for WHC-700 and 3.64–3.93 for WHC-800, in comparison to 3.59–3.67 for commercial Pt/C. In other words, similar to Pt/C, WHC-700 and WHC-800 catalyzed ORR mostly via the four-electron reduction route.

Further insights into the ORR electron-transfer kinetics might be obtained by Koutecky–Levich analysis, where the voltammetric current density (J) included both diffusion (J_d) and kinetic (J_k)-controlled components,[37–39]

$$\frac{1}{J} = \frac{1}{J_k} + \frac{1}{J_d} = \frac{1}{J_k} + \frac{1}{B\omega^{1/2}} \quad (2a)$$

$$B = 0.62 n F D^{2/3} \nu^{-1/6} C_{O_2} \quad (2b)$$

where F is the Faradaic constant (96 485 C mol^{-1}), C_{O_2} is the oxygen concentration in 0.1 M KOH (1.2×10^{-6} mol cm^{-3}), D is the oxygen diffusion coefficient in 0.1 M KOH (1.90×10^{-5} cm^2 s^{-1}), ν is the kinematic viscosity of the electrolyte solution (0.01 cm^2 s^{-1}), and ω is the electrode rotation rate.[40] The Koutecky–Levich plots (J^{-1} vs. $\omega^{-1/2}$) of WHC-700 at different electrode potentials were displayed in panel (e) and those of WHC-600 and WHC-800 were included in Fig. S3c and d,† where linear regressions showed good linearity with a rather consistent slope, suggesting first order reaction of ORR with respect to the concentration of oxygen dissolved in the solution. Furthermore, from the linear regressions, the kinetic components (J_k) might be quantified from the intercepts, which were depicted in the Tafel plot of panel (f). It can be seen that all samples exhibited a clear increase of the kinetic current density with increasingly negative electrode potential. For instance, the kinetic current density at +0.80 V is 1.04 mA cm^{-2}

for WHC-700, markedly higher than 0.21 mA cm^{-2} for WHC-600 and 0.59 mA cm^{-2} for WHC-800. In addition, all three WHC samples exhibited a similar Tafel slope, 107.2 mV dec^{-1} for WHC-600, 103.4 mV dec^{-1} for WHC-700 and 106.5 mV dec^{-1} for WHC-800, suggesting that the rate-determining step for ORR was the first electron reduction of oxygen at these carbon catalysts.[41]

It should be noted that the performance of the porous carbons prepared above is markedly better than or at least comparable to the leading results in the literature that are based on biomass-derived carbon for ORR, within the context of onset potential, number of electron transfer, durability and resistance against methanol crossover.[9,16,41–46] The comparison is detailed in Table S1.†[9,16,42–47]

The porous carbons also exhibited excellent resistance against methanol crossover and remarkable long-term stability in continuous operation. Experimentally, the tolerance of WHC-700 to methanol crossover was assessed by chronoamperometric measurements with the potential set at +0.4 V and a rotation speed of 900 rpm in O$_2$-saturated 0.1 M KOH, in comparison to that of the commercial Pt/C catalyst. As shown in Fig. 5a, when 3 M methanol was introduced into the electrochemical cell, the WHC-700 catalyst retained a virtually invariant current response, indicating its excellent catalytic selectivity for ORR against methanol oxidation. In contrast, the relative current of commercial Pt/C showed a sharp loss of about 60% in activity. The durability of WHC-700 and Pt/C were also compared. From Fig. 5b, it can be seen that after 30 000 s of continuous operation, the ORR performance of WHC-700 displayed a very small attenuation of only 8.8%, in contrast to 17.8% for Pt/C under the same experimental conditions. These results suggest that the WHC-700 catalyst possessed significantly better stability than Pt/C.

Conclusions

In this work, we developed a facile, cost-effective approach based on pyrolysis at controlled temperatures to the fabrication of novel N-self-doped carbons with a high surface area from water hyacinth, a natural, abundantly available, and renewable biomass that acted as a single precursor for both carbon and heteroatoms, therefore eliminating the need of hazardous chemicals in the synthetic processes. The obtained N-doped carbons all exhibited apparent electrocatalytic activity for ORR, and the optimal pyrolysis temperature was identified at 700 °C, where the corresponding sample (WHC-700) exhibited the best electrocatalytic performance among the series, with high selectivity and long durability, in comparison to leading commercial Pt/C catalysts. This may be accounted for by the highest concentration of pyridinic and graphitic nitrogens in the WHC-700 sample. The results demonstrated that simple pyrolysis of water hyacinth might be a viable route towards the preparation and engineering of functional carbons as metal-free ORR electrocatalysts for alkaline fuel cells.

Notes and references

1 J. Greeley, I. E. L. Stephens, A. S. Bondarenko, T. P. Johansson, H. A. Hansen, T. F. Jaramillo, J. Rossmeisl, I. Chorkendorff and J. K. Nørskov, *Nat. Chem.*, 2009, **1**, 552–556.

2 Z.-H. Sheng, H.-L. Gao, W.-J. Bao, F.-B. Wang and X.-H. Xia, *J. Mater. Chem.*, 2012, **22**, 390–395.

3 Q. Liu, Y. Duan, Q. Zhao, F. Pan, B. Zhang and J. Zhang, *Langmuir*, 2014, **30**, 8238–8245.

4 Y. Tang, B. L. Allen, D. R. Kauffman and A. Star, *J. Am. Chem. Soc.*, 2009, **131**, 13200–13201.

5 X. a. Chen, X. Chen, X. Xu, Z. Yang, Z. Liu, L. Zhang, X. Xu, Y. Chen and S. Huang, *Nanoscale*, 2014, **6**, 13740–13747.

6 Q. Shi, F. Peng, S. Liao, H. Wang, H. Yu, Z. Liu, B. Zhang and D. Su, *J. Mater. Chem. A*, 2013, **1**, 14853–14857.

7 X. Ma, G. Ning, C. Qi, C. Xu and J. Gao, *ACS Appl. Mater. Interfaces*, 2014, **6**, 14415–14422.

8 C. H. Choi, S. H. Park and S. I. Woo, *ACS Nano*, 2012, **6**, 7084–7091.

9 F. Liu, H. Peng, C. You, Z. Fu, P. Huang, H. Song and S. Liao, *Electrochim. Acta*, 2014, **138**, 353–359.

10 H.-J. Liu, X.-M. Wang, W.-J. Cui, Y.-Q. Dou, D.-Y. Zhao and Y.-Y. Xia, *J. Mater. Chem.*, 2010, **20**, 4223–4230.

11 W. Huang, H. Zhang, Y. Huang, W. Wang and S. Wei, *Carbon*, 2011, **49**, 838–843.

12 K. Wang, H. Wang, S. Ji, H. Feng, V. Linkov and R. Wang, *RSC Adv.*, 2013, **3**, 12039–12042.

13 J. Zhang, S. Wu, X. Chen, K. Cheng, M. Pan and S. Mu, *RSC Adv.*, 2014, **4**, 32811–32816.

14 S. Gao, K. Geng, H. Liu, X. Wei, M. Zhang, P. Wang and J. Wang, *Energy Environ. Sci.*, 2015, **8**, 221–229.

15 F. Pan, Z. Cao, Q. Zhao, H. Liang and J. Zhang, *J. Power Sources*, 2014, **272**, 8–15.

16 K. N. Chaudhari, M. Y. Song and J.-S. Yu, *Small*, 2014, **10**, 2625–2636.

17 C. C. Gunnarsson and C. M. Petersen, *Waste Manage.*, 2007, **27**, 117–129.

18 C. Boyd, *Econ. Bot.*, 1970, **24**, 95–103.

19 J. Wooten and J. Dodd, *Econ. Bot.*, 1976, **30**, 29–37.

20 H. Peng, F. Liu, X. Liu, S. Liao, C. You, X. Tian, H. Nan, F. Luo, H. Song, Z. Fu and P. Huang, *ACS Catal.*, 2014, **4**, 3797–3805.

21 C. Hu, Y. Xiao, Y. Zhao, N. Chen, Z. Zhang, M. Cao and L. Qu, *Nanoscale*, 2013, **5**, 2726–2733.

22 W. Qian, F. Sun, Y. Xu, L. Qiu, C. Liu, S. Wang and F. Yan, *Energy Environ. Sci.*, 2014, **7**, 379–386.

23 M. Li, X. Bo, Y. Zhang, C. Han, A. Nsabimana and L. Guo, *J. Mater. Chem. A*, 2014, **2**, 11672–11682.

24 H. Zhong, C. Deng, Y. Qiu, L. Yao and H. Zhang, *J. Mater. Chem. A*, 2014, **2**, 17047–17057.

25 L.-F. Chen, X.-D. Zhang, H.-W. Liang, M. Kong, Q.-F. Guan, P. Chen, Z.-Y. Wu and S.-H. Yu, *ACS Nano*, 2012, **6**, 7092–7102.

26 H. Zhu, X. Wang, X. Liu and X. Yang, *Adv. Mater.*, 2012, **24**, 6524–6529.

27 H. Zhong, H. Zhang, S. Liu, C. Deng and M. Wang, *ChemSusChem*, 2013, **6**, 807–812.

28 T. Kondo, S. Casolo, T. Suzuki, T. Shikano, M. Sakurai, Y. Harada, M. Saito, M. Oshima, M. Trioni, G. Tantardini and J. Nakamura, *Phys. Rev. B: Condens. Matter*, 2012, **86**, 035436.

29 M. Liu, Y. Song, S. He, W. W. Tjiu, J. Pan, Y.-Y. Xia and T. Liu, *ACS Appl. Mater. Interfaces*, 2014, **6**, 4214–4222.

30 K. Stańczyk, R. Dziembaj, Z. Piwowarska and S. Witkowski, *Carbon*, 1995, **33**, 1383–1392.

31 L. Lai, J. R. Potts, D. Zhan, L. Wang, C. K. Poh, C. Tang, H. Gong, Z. Shen, J. Lin and R. S. Ruoff, *Energy Environ. Sci.*, 2012, **5**, 7936–7942.

32 H. Kim, K. Lee, S. I. Woo and Y. Jung, *Phys. Chem. Chem. Phys.*, 2011, **13**, 17505–17510.

33 D. Geng, Y. Chen, Y. Chen, Y. Li, R. Li, X. Sun, S. Ye and S. Knights, *Energy Environ. Sci.*, 2011, **4**, 760–764.

34 G. Liu, X. Li, J.-W. Lee and B. N. Popov, *Catal. Sci. Technol.*, 2011, **1**, 207–217.

35 J. Liang, Y. Jiao, M. Jaroniec and S. Z. Qiao, *Angew. Chem., Int. Ed.*, 2012, **51**, 11496–11500.

36 Z. Chen, W. Ren, L. Gao, B. Liu, S. Pei and H.-M. Cheng, *Nat. Mater.*, 2011, **10**, 424–428.

37 Y. Li, M. Gong, Y. Liang, J. Feng, J.-E. Kim, H. Wang, G. Hong, B. Zhang and H. Dai, *Nat. Commun.*, 2013, **4**, 1805.

38 G. Wu, K. L. More, C. M. Johnston and P. Zelenay, *Science*, 2011, **332**, 443–447.

39 H. Wang, Y. Liang, Y. Li and H. Dai, *Angew. Chem., Int. Ed.*, 2011, **50**, 10969–10972.

40 P. Chen, T.-Y. Xiao, Y.-H. Qian, S.-S. Li and S.-H. Yu, *Adv. Mater.*, 2013, **25**, 3192–3196.

41 C. Lin, Y. Song, L. Cao and S. Chen, *ACS Appl. Mater. Interfaces*, 2013, **5**, 13305–13311.

42 C.-Z. Guo, W.-L. Liao and C.-G. Chen, *J. Power Sources*, 2014, **269**, 841–847.

43 J. Li, S. Wang, Y. Ren, Z. Ren, Y. Qiu and J. Yu, *Electrochim. Acta*, 2014, **149**, 56–64.

44 C.-Z. Guo, C.-G. Chen and Z.-L. Luo, *J. Power Sources*, 2014, **245**, 841–845.

45 R. Wang, H. Wang, T. Zhou, J. Key, Y. Ma, Z. Zhang, Q. Wang and S. Ji, *J. Power Sources*, 2015, **274**, 741–747.

46 R. Gokhale, S. M. Unni, D. Puthusseri, S. Kurungot and S. Ogale, *Phys. Chem. Chem. Phys.*, 2014, **16**, 4251–4259.

47 J. Lu, X. Bo, H. Wang and L. Guo, *Electrochim. Acta*, 2013, **108**, 10–16.